# Atomic Imaging of Oxide-Supported Metallic Nanocrystals

**Zhenxing Feng,[†] Alexander Kazimirov,[§] and Michael J. Bedzyk[†,‡,⊥,*]**

[†]Department of Materials Science and Engineering, and [‡]Department of Physics and Astronomy, Northwestern University, Evanston, Illinois 60208, United States , [§]CHESS, Cornell University, Ithaca, New York 14853, United States , and [⊥]Materials Science Division, Argonne National Laboratory, Argonne, Illinois 60439, United States

**ABSTRACT** The nucleation of noble metal nanoparticles on oxide surfaces can lead to dramatic enhancements in catalytic activity that are related to the atomic-scale formation of the nanoparticles and interfaces. For the case of submonolayer Pt deposited on the 2×1 $SrTiO_3$(001) surface atomic-force microscopy shows the formation of nanoparticles. We use X-ray standing wave (XSW) atomic imaging to show that these nanoparticles are composed of Pt face-centered-cubic nanocrystals with cube-on-cube epitaxy laterally correlated to the substrate unit cell. The phase sensitivity of the XSW allows for a direct measurement of the interface offset between the two unit cells along the *c*-axis. Different Pt coverages lead to differences in the observed XSW image of the interfacial structure, which is explained by a proposed model based on the Pt−Pt interaction becoming stronger than the Pt−substrate interaction as the global coverage is increased from 0.2 to 0.6 ML.

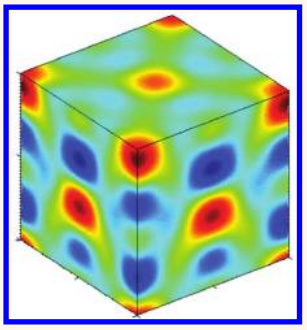

**KEYWORDS:** nanoparticles · epitaxy · atomic imaging · interface structure · X-ray standing waves · platinum · strontium titanate

Dramatically enhanced catalytic activities have been observed for a variety of noble metals in the form of nanoparticles supported on oxide surfaces.[1−4] The formation of metal nanoparticles is governed by the surface free energy, which is, in turn, determined by the atomic bonding across the interface between a particle and a supporting surface. Detailed structural information on multiple length scales, including the atomic scale, is required to gain insight into formation mechanisms and their links to catalytic activity.

A prime example is Pt on $SrTiO_3$ as a photocatalyst for water splitting.[1,2] The structure and resulting electronic properties of the Pt/$SrTiO_3$ interface are also of importance to thin-film technologies such as those used for dynamic random access memory devices.[5] Therefore, predictions of the metal/oxide interface structure, in general, would impact our understanding of numerous chemical and physical processes. Several theoretical investigations have predicted a complex interface structure at the atomic level for ultrathin film coverages from the submonolayer level to several monolayers.[6,7] Experimentally, direct imaging provides a way to look into the details of the interface structure of supported nanoparticles.

$SrTiO_3$ (STO) has a room-temperature (RT) lattice constant ($a$ = 3.905 Å, perovskite cubic-P crystal structure) close to that of Pt ($a$ = 3.924 Å, cubic-F). Cross-sectional transmission electron microscopy (TEM) and X-ray diffraction (XRD) studies of various growth methods for Pt on $SrTiO_3$(001) have shown that this close lattice match leads to Pt thin films with strain-relaxed cube-on-cube epitaxy to the substrate lattice, namely, $[001]_{Pt} \parallel [001]_{STO}$ and $[010]_{Pt} \parallel [010]_{STO}$.[8−10] There are also recent studies[11−13] of Pt nanoparticles grown on single-crystal STO nanocubes, which are important for catalysis applications due to the enormous gain in surface area.

In addition to electron microscopy, X-ray imaging techniques with 10−100 nm resolution have been initiated for *in situ* and/or real-time investigations of nanoparticles. Examples are X-ray coherent imaging of strain in supported nanocrystals,[14] nanoparticle imaging using ultrashort X-ray laser pulses,[15,16] and nanoscale structural imaging by resonant X-ray diffraction microscopy.[17] To complete the picture down to the level of interfacial bonding configurations requires element-specific, atomic-scale imaging of the supported nanoparticles. Herein, we show how this requirement can be met by X-ray standing wave (XSW) 3D atomic imaging, which has previously been applied to bulk impurities[18] and surface adsorbate atoms.[19,20] We use this nondestructive method to produce atomic-lattice images of supported nanoparticles

* Address correspondence to bedzyk@northwestern.edu.

Received for review August 24, 2011 and accepted October 27, 2011.

**Published online October 28, 2011**
**10.1021/nn203273e**

for the first time. Our case study is for the early (low coverage) stages of the nucleation and growth of Pt nanoparticles on the $TiO_2$-terminated surface of $SrTiO_3$(001).

Single-crystal XSW experiments[21−24] use a selected $H = hkl$ strong Bragg reflection to generate an $E$-field intensity pattern with the periodicity of the diffraction planes ($d_H$). Advancing in Bragg angle through this arc-second-wide reflection causes the antinodal planes of the XSW to shift inward by one-half of a $d$-spacing, which induces modulations in the characteristic X-ray fluorescence (XRF) signals from atoms above and below the substrate single-crystal surface. In simple terms the phase of this measured modulation is sensitive to the $\Delta d/d$ positions of the XRF-selected atoms relative to the diffraction planes, and the modulation amplitude senses the fraction of atoms at (or distribution about) this position. More rigorously the modulation measures the model-independent Fourier phase ($P_H$) and amplitude ($f_H$) for the distribution of XRF-selected atoms. By Fourier summation we produce 3D maps for the surface-deposited Pt and bulk Ti atomic distributions that are used to register (correlate) the Pt lattice relative to the $SrTiO_3$ lattice. This includes a determination of the interfacial offset between the Pt and $SrTiO_3$ unit cells along the $c$-axis and an estimation of the Pt occupation fractions for different lattice sites.

## RESULTS AND DISCUSSION

Following well-established surface preparation procedures,[25,26] two separate $SrTiO_3$(001) single-crystal substrates were cleaned, etched, and then $O_2$ annealed to obtain atomically flat, $TiO_2$-terminated surfaces. The substrates were then loaded into an ultra-high-vacuum (UHV) chamber located at the Advanced Photon Source 12ID-D station.[27] The chamber (Figure S1 in the Supporting Information) was equipped with molecular-beam epitaxy (MBE), low-energy electron diffraction (LEED), Auger electron spectroscopy, and XSW facilities. After annealing to 950 °C for 30 min, the $SrTiO_3$(001) surfaces revealed a two-domain 2×1 LEED pattern, as shown in Figure 1a. Surface XRD- and TEM-based models for the 2×1 reconstructed surface propose an extra $TiO_2$ layer atop the $TiO_2$-terminated $SrTiO_3$(001) surface.[28−30] Pt was then deposited from an e-beam evaporator onto the $SrTiO_3$(001) surface with the substrate at 400 °C. On the basis of X-ray fluorescence (with Rutherford backscattering calibration), the substrate with a 10 min Pt deposition time had a Pt coverage of $\Theta = 0.60$ monolayers (ML), and for the substrate with 2 min deposition time, $\Theta = 0.17$ ML. (1.00 ML = 6.58 atoms/nm$^2$.) These as-deposited surfaces retained the sharp 1×1 LEED spots, but weaker half-order spots, as shown in Figure 1b. After a series of annealing steps at increasing

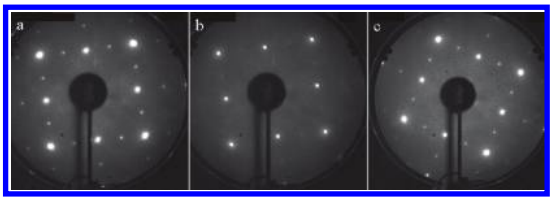


**Figure 1. Low-energy electron diffraction (LEED) patterns for (a) the clean $SrTiO_3$(001) surface after the UHV annealing treatment to obtain the two-domain 2×1 surface reconstruction, (b) the as-deposited 0.60 ML Pt/$SrTiO_3$ (001) surface, and (c) the 0.60 ML Pt/$SrTiO_3$(001) surface after the 910 °C anneal. The electron beam voltage was set at 65 V for each collected LEED pattern.**

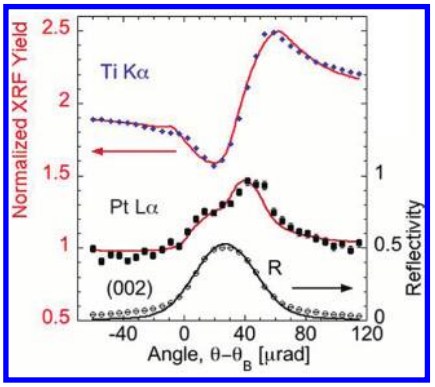


**Figure 2. *Ex situ* (002) XSW results show the angular dependence of the experimental data (symbols) and fitted curves (lines) for reflectivity and fluorescent yields of Pt Lα and bulk Ti Kα. The Ti yield is shifted vertically by +1 for clarity.**

temperatures that ended at 910 °C, the 2×1 sharp LEED pattern was recovered, as shown in Figure 1c. Previously published atomic-force microscopy (AFM) studies of similarly grown ML coverage Pt on $SrTiO_3$(001) show a surface morphology with nanoparticle formation.[29]

Using an incident X-ray energy of 12.50 keV, UHV RT XSW measurements were made for the as-deposited surface and after each annealing step for the 0.60 and 0.17 ML Pt/$SrTiO_3$(001) samples. These *in situ* XSW measurements were restricted to observing the modulation in the Pt Lα and Ti K XRF yields while scanning the incident angle through the $SrTiO_3$(002) Bragg peak. *Ex situ,* open-air, XSW measurements (Figure 2) were then made on each sample with a four-circle diffractometer, positioned just upstream of the UHV chamber. This goniometer allowed the single-crystal substrate to be rotated to several different selected *hkl* $SrTiO_3$ Bragg peaks as required for a complete 3D triangulation (or imaging) of the Pt atomic distribution relative to the substrate lattice. The surfaces were then examined by AFM, which showed nanoparticles supported on a surface with flat terraces separated by atomic steps (see Supporting Information). This morphology is consistent with similarly prepared Pt/$SrTiO_3$(001) surfaces.[26]

**TABLE 1. For the 0.60 ML Pt/$SrTiO_3$(001) Case: XSW-Measured $H = hkl$ Fourier Amplitudes, $f_H$, and Phases, $P_H$, for Pt[a]**

| | Pt measured | | Pt calculated | |
|---|---|---|---|---|
| *hkl* | $f_H$ | $P_H$ | $f_H$ | $P_H$ |
| 001 | 0.07(3) | | 0.07 | 0.07 |
| 002 | 0.39(3) | −0.18(2) | 0.32 | −0.15 |
| 011 | 0.07(3) | | 0.06 | 0.07 |
| 022 | 0.22(3) | −0.16(2) | 0.23 | −0.15 |
| 111 | 0.35(3) | −0.13(2) | 0.37 | −0.07 |
| 222 | 0.15(3) | −0.08(5) | 0.16 | −0.15 |

[a] The calculated values for Pt are determined from the best fit of the model described in eq 2.

**TABLE 2. XSW-Measured Fourier Amplitudes, $f_H$, and Phases, $P_H$, for the Bulk Ti Sublattice of $SrTiO_3$(001)[a]**

| *hkl* | 001 | 002 | 011 | 022 | 111 | 222 |
|---|---|---|---|---|---|---|
| *f* | 0.68(3) | 0.60(3) | 0.59(3) | 0.49(3) | 0.55(3) | 0.55(3) |
| *P* | 0.50(1) | 0.00(1) | 0.00(1) | 0.00(1) | 0.50(1) | 0.00(1) |
| α° | 8 | 11 | 48 | 40 | 40 | 41 |
| exp(−*M*) | 0.98 | 0.92 | 0.96 | 0.85 | 0.94 | 0.78 |
| *f*/exp(−*M*) | 0.69 | 0.65 | 0.61 | 0.58 | 0.59 | 0.71 |

[a] The takeoff angle (α) of the detected Ti Kα XRF emission relative to the surface is also listed. The *P* values are referenced to the Sr atom at the origin. $\exp(-M) = \exp(-2(\pi\sigma/d_H)^2)$ is the Debye−Waller factor, where $\sigma = 0.12$ Å is the thermal vibrational amplitude of the Ti atom at RT.

For the 0.60 ML Pt/$SrTiO_3$(001) sample the *ex situ* XSW measured values for the (002) Fourier amplitude, $f_{002} = 0.39$, and phase, $P_{002} = -0.18$, agree with the *in situ* UHV measured values (see Supporting Information). This strongly indicates the stability of this surface against oxidation and the reliability for attributing the atomic-scale structural results for the *ex situ* surface to the *in situ* surface. Figure 2 shows the XSW data and fit for the $SrTiO_3$(002) Bragg peak. The surface Pt Lα and bulk Ti Kα XRF yields are both analyzed. Due to diffuse (incoherent) scattering, the tails of the experimental reflectivity (rocking) curve are higher than the theory for a perfect single crystal. Table 1 and Table 2 list the entire *ex situ* measured set of $f_H$ and $P_H$ values of Pt and Ti for the 0.60 ML sample, respectively. The summation of these two sets of XSW-measured Fourier components (and their symmetry equivalents) produce model-independent 3D maps[18,31] of the Pt and Ti atomic distributions,

$$\rho(\mathbf{r}) = 1 + 2 \sum_{\mathbf{H}\neq -\mathbf{H},\, \mathbf{H}\neq 0} f_H \cos(2\pi P_H - \mathbf{H}\cdot\mathbf{r}) \quad (1)$$

Figure 3a and c show, respectively, the Pt and Ti 3D atomic maps for the 0.60 ML sample as referenced to the $SrTiO_3$ substrate unit cell with Sr positions at the corners of the cube. As expected the Ti shows up in the body-centered position. Due to the Fourier summation process, the XSW maps have the 3D periodicity of the substrate primitive unit cell. What was not obvious from studying the values in Table 1, but becomes immediately obvious by their subsequent Fourier summation, is that the Pt atoms form a face-centered-cubic (fcc) lattice that is registered to the substrate unit cell, namely, $[001]_{Pt} \parallel [001]_{STO}$ and $[010]_{Pt} \parallel [010]_{STO}$. Furthermore, one sees that the Pt density maxima are shifted vertically inward relative to the Sr sublattice, by $\sim(1/10)a_{STO} = 0.4$ Å.

To better understand the Pt 3D map, a 1D projection along the *c*-axis is shown in Figure 3b. The $\Delta z = 0.25$ fwhm of the two peaks corresponds to 1/2 $d_{002}$, which is the resolution of the measurement due to truncation

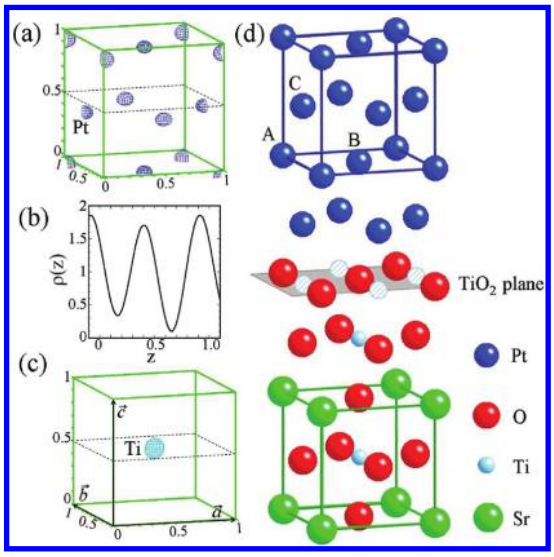


**Figure 3. For the 0.60 ML Pt/$SrTiO_3$(001) interface: (a) XSW-measured model-independent 3D Pt atomic map. The outlined green cubes are the $SrTiO_3$ unit cell with Sr at the corners (origin). (b) Projection of the 3D density along the *c*-axis to produce a 1D Pt atomic density as a function of the fractional *c*-axis coordinate, *z*, for the $SrTiO_3$ unit cell. (c) XSW-measured 3D Ti atomic density map. The contour plots in (a) and (c) are at 80%. (d) Proposed interface atomic model of fcc Pt on a double-layer $TiO_2$-terminated $SrTiO_3$-(001) surface, where A, B, and C refer to the three symmetry-inequivalent Pt sites. The striped light blue spheres in the extra $TiO_2$ layer represent Ti sites that are on average 50% occupied due to the two-domain 2×1 reconstruction of the surface.**

of the Fourier summation at $hkl = 002$. The two peaks have nearly equal density (occupation) and are spaced by 1/2 $a_{STO}$. This corresponds to Pt in a nearly perfect fcc atomic arrangement, for which $f_{001} \approx 0$ (analogous to structure factor $F_{001} = 0$ for fcc). As will be discussed later, this is different from the 0.17 ML case, where a value significantly greater than zero, $f_{001} = 0.21$, was measured.

Figure 3d shows a proposed interface atomic model for explaining the observed 0.60 ML 3D Pt density map. This is based on the 2×1 reconstructed double layer (DL) model,[28−30] in which one extra $TiO_2$ layer is added to the $TiO_2$-terminated $SrTiO_3$(001) surface. For this fcc-like Pt unit cell there are three types of

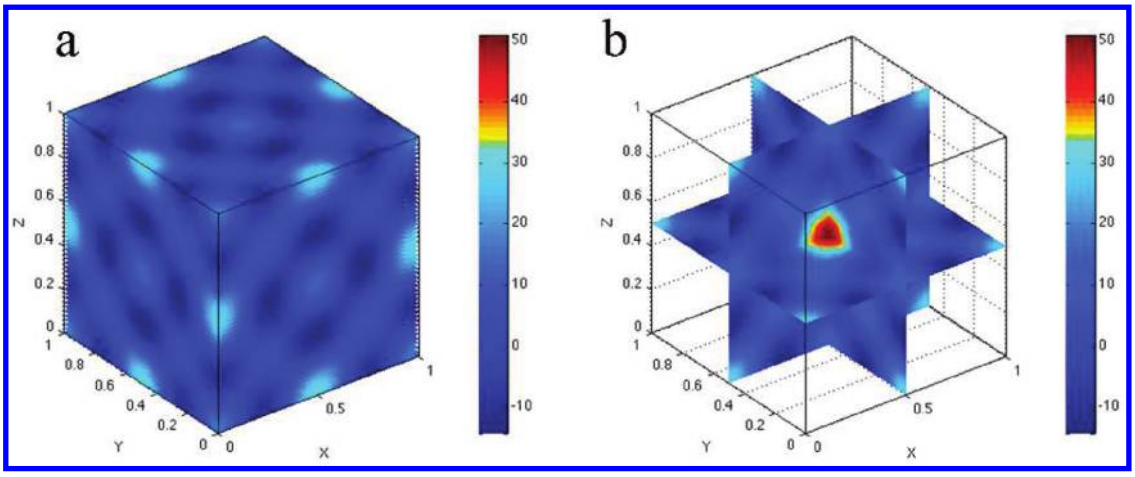


**Figure 4. 2D plane-cuts through 3D titanium atomic density map along the (a) outer surfaces of the $SrTiO_3$ unit cell and (b) interior surfaces of the unit cell. The map is generated by the summation of XSW-measured (*hkl*) Fourier components listed in Table 2 plus their symmetry equivalents.**

symmetry-inequivalent adsorption sites on the $SrTiO_3$-(001) surface: the corner site (A site), base-center site (B site), and the two symmetry-equivalent side-center sites (C site).[32] To better quantify the Pt occupation fractions ($c_X$) and heights ($h_X = a_{STO} \cdot z_X$) above the bulk-like SrO plane for the three sites, we used a least-squares global fit of the proposed model to the set of measured Fourier components,

$$F_H = f_H e^{2\pi i P_H} = e^{-2(\pi\sigma/d_H)^2}\{c_A e^{2\pi i \mathbf{H}\cdot\mathbf{r_A}} + c_B e^{2\pi i \mathbf{H}\cdot\mathbf{r_B}} + c_C[e^{2\pi i \mathbf{H}\cdot\mathbf{r_{C1}}} + e^{2\pi i \mathbf{H}\cdot\mathbf{r_{C2}}}]\} \quad (2)$$

where vectors $r_A = (0,0,z_A)$, $r_B = (1/2,1/2,z_B)$, $r_{C1} = (1/2,0,1/2+z_C)$, and $r_{C2} = (0,1/2,1/2+z_C)$ locate the four Pt sites relative to the substrate unit cell origin and $\sigma$ is the width of the Pt distribution (assumed to be isotropic) about these sites. The best-fit determined results are $c_A = 0.16$, $c_B = 0.11$, $c_C = 0.11$, $h_A = 7.69$ Å, $h_B = 7.44$ Å, $h_C = 5.49$ Å, and $\sigma = 0.26$ Å, which agree very well with the numerical analysis of the model-independent 3D map (Figure S10 in the Supporting Information). The occupation ratio between the three sites ($c_A$:$c_B$:$c_C \approx$ 3:2:2) is reasonably close to the ratio of an ideal fcc arrangement (1:1:1), where there are an equal number of Pt atoms in each layer.

Results also show that $c_A + c_B + 2c_C = 0.49$. Normally for a highly perfect single-crystal substrate, such as Si or Ge, this would mean that only 49% of the Pt atoms are correlated with the substrate lattice. However, this is not a perfect single-crystal substrate, as the diffuse tails of the measured reflectivity (Figure 2) indicate. Using XSW analysis of the Ti sublattice within bulk $SrTiO_3$(001) as a reference, we determine that 0.78 is a better estimation of Pt correlation fraction. (See Figure S11 and discussion in the Supporting Information.) The Ti Kα XRF yield was collected simultaneously with the Pt signal (Figure S2 in the Supporting Information). The analysis results are listed in Table 2. The XRF takeoff angle, α, relative to the sample surface is used to calculate the effective thickness of the Ti Kα fluorescence signal, which includes the extinction effect.[24] (As an example, the effective thickness sampled by the Ti K XRF yield for the 002 XSW measurement varies from 2.9 $\mu$m at the off-Bragg wings of the reflection to 0.5 $\mu$m at the center of the Bragg reflection.) By inserting the measured coherent fractions and positions (*i.e.*, Fourier amplitudes and phases) of bulk Ti into eq 1, a Ti atomic density map is generated, as shown in Figure 4 and Figure 3c. As it should be, the Ti density maximum is located in the center of the $SrTiO_3$ cubic unit cell. This further validates our XSW analysis procedure. The much weaker subsidiary maxima in the 3D map of Figure 4 are due to the truncation of the Fourier summation.

For the 0.17 ML case, the XSW-measured 3D Pt density map, Figure 5a, also shows an fcc-like structure, but with a vertical shift of $\sim(1/2)a_{STO}$. This is quite different from the 0.60 ML case shown in Figure 3a. Therefore, a different interface model is proposed in Figure 5c that shows the first layer of Pt directly above the O atoms in the DL $TiO_2$-terminated $SrTiO_3$. Model-independent and model-dependent analyses (see Supporting Information) both show that the Pt occupation fraction ratio of the three sites is $c_A$:$c_B$:$c_C$ = 2:2:1. Unlike the 0.60 ML case, this indicates that at 0.17 ML there are twice as many Pt atoms in the layer containing the A and B sites as in the neighboring layer containing the C site. The 1D projection of this Pt atomic density along the *c*-axis (Figure 5b) also shows a significant deviation in layer spacing from the ideal fcc arrangement; that is, the two layers have a vertical spacing of $0.4a_{STO}$, rather than $(1/2)a_{STO}$ (see Supporting Information).

The Pt/$SrTiO_3$(001) interface structures observed by XSW can be attributed to the $SrTiO_3$(001) surface termination, Pt-support interactions, and Pt−Pt interactions. Earlier experimental[28,30] and theoretical[29,33]

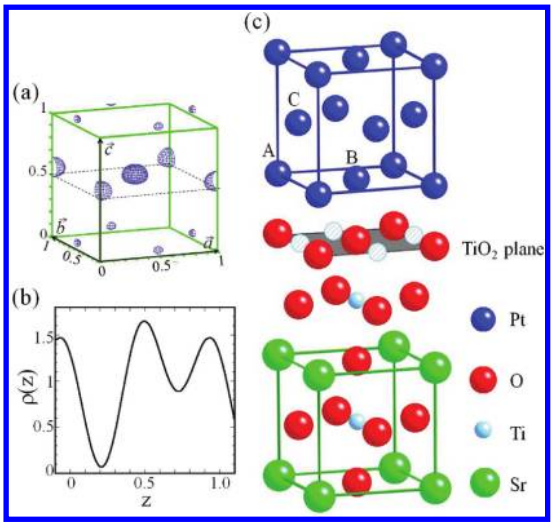


**Figure 5. For the 0.17 ML Pt/$SrTiO_3$(001) interface: (a) 3D XSW-measured Pt atomic density map as referenced to the $SrTiO_3$ unit cell with Sr positions at the corners (origin). (b) Projection of 3D Pt density along the *c*-axis. (c) Proposed atomic interface model.**

studies of the bare 2×1 $SrTiO_3$(001) surface support the formation of a double-layer (DL) $TiO_2$-terminated surface. We found no reported theory predictions for Pt on the DL $TiO_2$-terminated surface. However, density functional theory (DFT) calculations for very low Pt coverages on $TiO_2$-terminated $SrTiO_3$(001) predict that the Pt–support interaction is stronger than the Pt–Pt interaction,[7] and Pt atoms strongly prefer to adsorb on top of the O atoms.[6,7] Furthermore, DFT calculations by Asthagiri and Sholl[7] show that as the Pt coverage increases from 0.5 to 1 ML on the $TiO_2$-terminated $SrTiO_3$(001) surface, the Pt–substrate bond is weakened due to additional Pt–Pt bonds on the surface. For 1 ML this same DFT study proposes that interface Pt atoms would prefer to bind above Ti sites on the $TiO_2$-terminated surface to continue the fcc-like packing.[7] This leads to the interface structure model proposed in Figure 3d for the 0.60 ML case. The equal occupation of the three symmetry-inequivalent sites further indicates that the Pt nanoclusters seen in the AFM are primarily built from multiple layers of Pt. The AFM analysis shows that the average Pt nanocluster height is ~1.5 nm for the 0.60 ML case, which is reasonably consistent with our atomic model and the equal-occupied multiple layer structures. For the 0.17 ML case this AFM measured average height is ~1 nm. From our measurements of the 0.17 ML Pt/$SrTiO_3$(001) interface, we propose that a significant fraction of first-layer Pt atoms are not capped off with additional Pt layers. This could lead to a stronger Pt–O interaction as proposed with the interface model shown in Figure 5c.

## CONCLUSIONS

In summarizing this first XSW imaging of atoms in supported nanoparticles, we observed the fcc cube-on-cube epitaxial structure for submonolayer Pt grown on $SrTiO_3$(001) surfaces by MBE. We experimentally show for the first time that two different interface structures of Pt are formed with different initial Pt coverages, which could be further explained by the surface termination of $SrTiO_3$(001) and the interactions of Pt–Pt and Pt–support. Our proposed atomic-scale interface models, which start with a $TiO_2$ double-layer $SrTiO_3$(001) surface, indicate that at a very low coverage (0.17 ML) Pt prefers to bond on top of the O atoms due to the strong Pt–support interaction. However, at a higher coverage (0.60 ML) taller Pt nanocrystals are formed with stronger Pt–Pt interaction, which causes the interface Pt atoms to bond above Ti atomic sites. Equal occupation in the three symmetry-inequivalent sites indicates those Pt nanocrystals have two or more complete Pt layers locally, which is in contrast to our finding of unequally occupied layers for the 0.17 ML case. This atomic-level metal/perovskite interface study is important for understanding subsequent physical and chemical properties in electronic and catalytic applications.

## METHODS

**Preparation of Substrates.** Strontium titanate ($SrTiO_3$) single crystals were oriented, cut (10 × 10 × 1 $mm^3$), and polished parallel to the (001) by OKEN (Japan). $SrTiO_3$(001) substrates were ultrasonicated for 10 min in deionized water (18 MΩ/cm) and subsequently etched in a hydrofluoric acid buffer solution for approximately 30 s. The substrates were then rinsed in deionized water and dried in Ar gas. To produce atomically flat terraces terminated with titanium oxide,[25,26,34] the substrates were loaded into a tube furnace with $O_2$ flow (~100 sccm) and annealed at 1050 °C for 5 h. After annealing in $O_2$, the substrates were mounted on a tantalum sample plate using spot-welded tantalum wire and loaded into an X-ray Surface Science ultra-high-vacuum multichamber (Figure S1 in the Supporting Information) located at the 12ID-D undulator BESSRC-CAT station at the Advanced Photon Source (APS), Argonne National Laboratory. The vacuum chamber was maintained at a base pressure of $2 \times 10^{-10}$ Torr and equipped with a reverse-view low-energy electron diffraction (LEED; PHI), Auger electron spectroscopy (AES: PHI), and an electron-beam evaporator source (Omicron).

**Platinum Growth.** Prior to platinum deposition, the substrates were annealed at 950 °C for 30 min in the UHV chamber using a resistive tungsten filament heater placed behind the sample. Auger analysis showed clean surfaces with negligible carbon contamination. A 1.5 mm diameter Pt rod was placed inside the e-beam evaporator to deposit Pt thin films. Platinum was deposited onto the atomically clean $SrTiO_3$ (STO) surface, which was held at 400 °C. After cooling to RT the "as deposited" (002) XSW measurement was made. The sample was then annealed to a series of increasing temperatures, cooled to RT, and given a 002 XSW measurement. The series of annealing temperatures were 0.5 h at 500 °C, 1 h at 700 °C, 1 h at 800 °C, and 1 h at 910 °C.

**Characterizations.** LEED measurements were taken before Pt deposition, after Pt deposition, and after the 910 °C annealing step.

XSW measurements were performed at the APS undulator station 12ID-D of BESSRC-CAT. An incident photon energy of 12.50 keV was selected with a Si(111) high-heat-load monochromator and conditioned further with a Si(004) channel-cut post-monochromator crystal. The incident beam slit was 20 $\mu$m high by 100 $\mu$m wide. Using this small X-ray spot it was possible to find lateral positions on the sample surface that produced reflectivity curves that reasonably matched dynamical diffraction theory predictions for a $SrTiO_3$ single crystal. A solid-state Si(Li) detector was used to collect the X-ray fluorescence spectra. An XRF-collected spectrum is shown in Figure S3 in the Supporting Information. The Pt coverages, 0.17 and 0.60 ML, were determined from a side-by-side XRF comparison to a Si implanted standard that was calibrated by Rutherford backscattering. One monolayer is defined as 6.58 atoms/nm$^2$.

*Acknowledgment.* This work was supported by the Institute for Catalysis in Energy Processes (U.S. DOE Grant DE-FG02-03ER15457) and MRSEC (NSF Grant DMR-0520513). X-ray measurements were performed at Argonne National Laboratory (U. S. DOE Grant DE-AC02-06CH11357). The authors are thankful for helpful discussions with and technical assistance from Steven Christensen, Stephen Streiffer, David Marasco, and Tien Lin Lee.

*Supporting Information Available:* Details of the experimental setup and XSW analysis. This material is available free of charge *via* the Internet at http://pubs.acs.org.

## REFERENCES AND NOTES

1. Carr, R. G.; Somorjai, G. A. Hydrogen-Production from Photolysis of Steam Adsorbed onto Platinized $SrTiO_3$. *Nature* **1981**, *290*, 576–577.
2. Ikeda, S.; Hirao, K.; Ishino, S.; Matsumura, M.; Ohtani, B. Preparation of Platinized Strontium Titanate Covered with Hollow Silica and its Activity for Overall Water Splitting in a Novel Phase-Boundary Photocatalytic System. *Catal. Today* **2006**, *117*, 343–349.
3. Rosseler, O.; Shankar, M. V.; Du, M. K. L.; Schmidlin, L.; Keller, N.; Keller, V. Solar Light Photocatalytic Hydrogen Production from Water over Pt and Au/$TiO_2$(anatase/rutile) Photocatalysts: Influence of Noble Metal and Porogen Promotion. *J. Catal.* **2010**, *269*, 179–190.
4. Chen, M. S.; Goodman, D. W. The Structure of Catalytically Active Gold on Titania. *Science* **2004**, *306*, 252–255.
5. Menke, T.; Dittmann, R.; Meuffels, P.; Szot, K.; Waser, R. Impact of the Electroforming Process on the Device Stability of Epitaxial Fe-doped $SrTiO_3$ Resistive Switching Cells. *J. Appl. Phys.* **2009**, *106*, 114507.
6. Iddir, H.; Komanicky, V.; Ogut, S.; You, H.; Zapol, P. Shape of Platinum Nanoparticles Supported on $SrTiO_3$: Experiment and Theory. *J. Phys. Chem. C* **2007**, *111*, 14782–14789.
7. Asthagiri, A.; Sholl, D. S. First Principles Study of Pt Adhesion and Growth on SrO- and $TiO_2$-Terminated $SrTiO_3$-(100). *J. Chem. Phys.* **2002**, *116*, 9914–9925.
8. Francis, A. J.; Salvador, P. A. Crystal Orientation and Surface Morphology of Face-Centered-Cubic Metal Thin Films Deposited upon Single-Crystal Ceramic Substrates Using Pulsed Laser Deposition. *J. Mater. Res.* **2006**, *22*, 89–102.
9. Polli, A. D.; Wagner, T.; Gemming, T.; Ruhle, M. Growth of Platinum on $TiO_2$- and SrO-Terminated $SrTiO_3$(100). *Surf. Sci.* **2000**, *448*, 279–289.
10. Son, J.; Cagnon, J.; Stemmer, S. Strain Relaxation in Epitaxial Pt Films on (001) $SrTiO_3$. *J. Appl. Phys.* **2009**, *106*, 043525.
11. Christensen, S. T.; Elam, J. W.; Rabuffetti, F. A.; Ma, Q.; Weigand, S. J.; Lee, B.; Seifert, S.; Stair, P. C.; Poeppelmeier, K. R.; Hersam, M. C.; *et al.* Controlled Growth of Platinum Nanoparticles on Strontium Titanate Nanocubes by Atomic Layer Deposition. *Small* **2009**, *5*, 750–757.
12. Enterkin, J. A.; Poeppelmeier, K. R.; Marks, L. D. Oriented Catalytic Platinum Nanoparticles on High Surface Area Strontium Titanate Nanocuboids. *Nano Lett.* **2011**, *11*, 993–997.
13. Enterkin, J. A.; Setthapun, W.; Elam, J. W.; Christensen, S. T.; Rabuffetti, F. A.; Marks, L. D.; Stair, P. C.; Poeppelmeier, K. R.; Marshall, C. L. Propane Oxidation over Pt/$SrTiO_3$ Nanocuboids. *ACS Catal.* **2011**, *1*, 629–635.
14. Robinson, I.; Harder, R. Coherent X-ray Diffraction Imaging of Strain at the Nanoscale. *Nat. Mater.* **2009**, *8*, 291–298.
15. Bogan, M. J.; Benner, W. H.; Boutet, S.; Rohner, U.; Frank, M.; Barty, A.; Seibert, M. M.; Maia, F.; Marchesini, S.; Bajt, S.; *et al.* Single Particle X-ray Diffractive Imaging. *Nano Lett.* **2008**, *8*, 310–316.
16. Timneanu, N.; Caleman, C. C., C.; Huldt, G.; Maia, F. R. N. C.; Ortiz, C.; Parak, F. G.; Hajdu, J.; van der Spoel, D.; Chapman, H. N. On the Feasibility of Nanocrystal Imaging Using Intense and Ultrashort X-ray Pulses. *ACS Nano* **2011**, *5*, 139–146.
17. Song, C. Y.; Bergstrom, R.; Ramunno-Johnson, D.; Jiang, H. D.; Paterson, D.; de Jonge, M. D.; McNulty, I.; Lee, J. Y.; Wang, K. L.; Miao, J. W. Nanoscale Imaging of Buried Structures with Elemental Specificity Using Resonant X-ray Diffraction Microscopy. *Phys. Rev. Lett.* **2008**, *100*, 025504.
18. Cheng, L.; Fenter, P.; Bedzyk, M. J.; Sturchio, N. C. Fourier-Expansion Solution of Atom Distributions in a Crystal Using X-ray Standing Waves. *Phys. Rev. Lett.* **2003**, *90*, 255503.
19. Okasinski, J. S.; Kim, C.; Walko, D. A.; Bedzyk, M. J. X-Ray Standing Wave Imaging of the 1/3 Monolayer Sn/Ge-(111) Surface. *Phys. Rev. B* **2004**, *69*, 041401(R).
20. Zhang, Z.; Fenter, P.; Cheng, L.; Sturchio, N. C.; Bedzyk, M. J.; Machesky, M. L.; Wesolowski, D. J. Model-Independent X-ray Imaging of Adsorbed Cations at the Crystal-Water Interface. *Surf. Sci.* **2004**, *554*, L95–L100.
21. Batterman, B. W. Detection of Foreign Atom Sites by Their X-Ray Fluorescence Scattering. *Phys. Rev. Lett.* **1969**, *22*, 703–705.
22. Golovchenko, J. A.; Patel, J. R.; Kaplan, D. R.; Cowan, P. L.; Bedzyk, M. J. Solution to the Surface Registration Problem Using X-Ray Standing Waves. *Phys. Rev. Lett.* **1982**, *49*, 560–563.
23. Zegenhagen, J. Surface-Structure Determination with X-Ray Standing Waves. *Surf. Sci. Rep.* **1993**, *18*, 199–271.
24. Bedzyk, M. J.; Cheng, L. X-ray Standing Wave Studies of Minerals and Mineral Surfaces: Principles and Applications. *Rev. Mineral. Geochem.* **2002**, *49*, 221–266.
25. Koster, G.; Rijnders, G.; Blank, D. H. A.; Rogalla, H. Surface Morphology Determined by (001) Single-Crystal $SrTiO_3$ Termination. *Phys. C (Amsterdam, Neth.)* **2000**, *339*, 215–230.
26. Christensen, S. T.; Lee, B.; Feng, Z.; Hersam, M. C.; Bedzyk, M. J. Hierarchical Nanoparticle Morphology for Platinum Supported on $SrTiO_3$ (001): A Combined Microscopy and X-ray Scattering Study. *Appl. Surf. Sci.* **2009**, *256*, 423–427.
27. Escuadro, A. A. X-ray Standing Wave Imaging of Metal Atoms on Semiconductor and Oxide Surfaces. Ph.D. Thesis, Northwestern University, Evanston, IL, 2005.
28. Erdman, N.; Poeppelmeier, K. R.; Asta, M.; Warschkow, O.; Ellis, D. E.; Marks, L. D. The Structure and Chemistry of the $TiO_2$-Rich Surface of $SrTiO_3$(001). *Nature* **2002**, *419*, 55–58.
29. Warschkow, O.; Asta, M.; Erdman, N.; Poeppelmeier, K. R.; Ellis, D. E.; Marks, L. D. $TiO_2$-Rich Reconstructions of $SrTiO_3$-(001): A Theoretical Study of Structural Patterns. *Surf. Sci.* **2004**, *573*, 446–456.
30. Herger, R.; Willmott, P. R.; Bunk, O.; Schlepuetz, C. M.; Patterson, B. D.; Delley, B. Surface of Strontium Titanate. *Phys. Rev. Lett.* **2007**, *98*, 076102.
31. Feng, Z.; Kim, C.-Y.; Elam, J. W.; Ma, Q.; Zhang, Z.; Bedzyk, M. J. Direct Atomic-Scale Observation of Redox-induced Cation Dynamics in an Oxide-Supported Monolayer Catalyst: WOx/$\alpha$-$Fe_2O_3$ (0001). *J. Am. Chem. Soc.* **2009**, *131*, 18200–18201.
32. Because the surface breaks the symmetry along *c*-axis, the bulk fcc symmetry-equivalent B and C sites become symmetry-inequivalent.
33. Johnston, K.; Castell, M. R.; Paxton, A. T.; Finnis, M. W. $SrTiO_3$(001)(2$\times$1) Reconstructions: First-Principles Calculations of Surface Energy and Atomic Structure Compared with Scanning Tunneling Microscopy Images. *Phys. Rev. B* **2004**, *70*, 085415.
34. Jiang, Q. D.; Zegenhagen, J. C(6$\times$2) and C(4$\times$2) Reconstruction of $SrTiO_3$(001). *Surf. Sci.* **1999**, *425*, 343–354.